Journal of Colloid and Interface Science 660 (2024) 989–996

Contents lists available at ScienceDirect

Journal of Colloid And Interface Science

journal homepage: www.elsevier.com/locate/jcis

Regular Article

Synergistic vacancy engineering of Co/MnO@NC catalyst for superior oxygen reduction reaction in liquid/solid zinc-air batteries

Lixia Wang [a], Jia Huang [a], Xinran Hu [a], Zhiyang Huang [a], Mingcheng Gao [a], Di Yao [a,*], Tayirjan Taylor Isimjan [b], Xiulin Yang [a,*]

[a] Guangxi Key Laboratory of Low Carbon Energy Materials, School of Chemistry and Pharmaceutical Sciences, Guangxi Normal University, Guilin 541004, China
[b] Saudi Arabia Basic Industries Corporation (SABIC) at King Abdullah University of Science and Technology (KAUST), Thuwal 23955-6900, Saudi Arabia

HIGHLIGHTS

- Spherical Co/MnO@NC is synthesized by a hydrothermal-pyrolysis strategy.
- The catalyst displays notable ORR activity ($J_L = 5.1$ mAcm^{-2}) comparable to Pt/C.
- Aqueous/solid-state ZABs exhibit high power density (217.7/63.3 mW cm^{-2}).
- Vacancies, conductivity and hydrophilicity dominate the delightful performance.

GRAPHICAL ABSTRACT

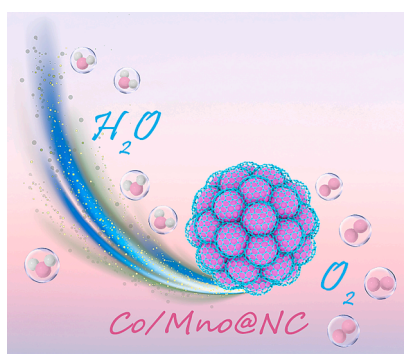

ARTICLE INFO

Keywords:
Co/MnO@NC
Vacancy
Oxygen reduction reaction
Liquid/solid Zinc-air batteries

ABSTRACT

The pursuit of efficient and economically viable catalysts for liquid/solid-state zinc-air batteries (ZABs) is of paramount importance yet presents formidable challenge. Herein, we synthesized a vacancy-rich cobalt/manganese oxide catalyst (Co/MnO@NC) stabilized on a nitrogen-doped mesoporous carbon (NC) nanosphere matrix by leveraging hydrothermal and high-temperature pyrolysis strategy. The optimized Co/MnO@NC demonstrates fast reaction kinetics and large limiting current densities comparable to commercial Pt/C in alkaline electrolyte for oxygen reduction reaction (ORR). Moreover, the Co/MnO@NC serves as an incredible cathode material for both liquid and flexible solid-state ZABs, delivering impressive peak power densities of 217.7 and 63.3 mW cm^{-2} and robust long-term stability (459 h), outperforming the state-of-the-art Pt/C and majority of the currently reported catalysts. Research indicates that the superior performance of the Co/MnO@NC catalyst primarily stems from the synergy between the heightened electrical conductivity of metallic Co and the regulatory capacity of MnO on adsorbed oxygen intermediates. In addition, the abundance of vacancies regulates the electronic configuration, and superhydrophilicity facilitates efficient electrolyte diffusion, thereby effectively ensuring optimal contact between the active site and reactants. Besides, the coexisting NC layer avoids the shedding of active sites, resulting in high stability. This work provides a viable approach for designing and advancing high-performance liquid/solid-state ZABs, highlighting the great potential of energy storage technology.

* Corresponding authors.
E-mail addresses: yaodi@gxnu.edu.cn (D. Yao), xlyang@gxnu.edu.cn (X. Yang).

https://doi.org/10.1016/j.jcis.2024.01.143
Received 21 December 2023; Received in revised form 12 January 2024; Accepted 21 January 2024
Available online 22 January 2024

1. Introduction

Zinc-air batteries (ZABs) hold immense promise as a sustainable energy technology due to their safe operation, eco-friendliness, high energy density (1086 Wh kg^{-1}), and economic viability [1,2]. The escalating demand for portable and wearable electronic devices underscores the imperative for high-performance energy storage and conversion systems [3,4]. The oxygen reduction catalyst plays a pivotal role in ZABs, impacting their cycling stability and lifespan. Unfortunately, the sluggish kinetics of the oxygen reduction reaction (ORR) at the ZAB cathode pose a significant challenge, hindering advancements in overall ZAB performance [5,6]. Contemporarily, the commercialization of ORR faces challenges due to the high cost and limited availability of precious metal catalysts such as Pt/C and RuO_2/IrO_2 [7,8]. Therefore, exploring non-precious metal alternatives is crucial to meet the growing need for sustainable energy [9,10].

Low-cost transition metals, including Fe, Co, Ni, and Mn based materials, have garnered attention for their remarkable electrocatalytic activity [11]. Among these, manganese-based materials stand out as a particularly promising option, boasting abundant reserves, affordable prices, and notable environmental friendliness [12]. The redox interaction between MnO_x facilitates charge transfer to oxygen species, promoting the efficient decomposition of peroxides (HO_2^-) [13]. Simultaneously, cobalt-based materials exhibit admirable catalytic activity and excellent tolerance in alkaline solution [14]. Moreover, surface-exposed carbon edge defects have proven effective in enhancing catalytic activity [15]. Despite significant progress, the limited affinity between transition metals and carbon carriers poses challenges to catalytic stability [16]. Addressing this, recent studies emphasize the pivotal role of synergistic integration between metals or metal oxides and nitrogen-doped carbon (NC) [17]. This integration protects active sites, enhancing catalyst stability and refining ORR kinetics [18]. Vacancies induce localized electronic and coordination unsaturation, finely tuning the catalyst's electronic structure and intrinsic catalytic activity [19]. These intrinsic defects do not introduce foreign elements, promoting structural integrity and durability [20]. Consequently, integrating carbon materials, introducing defects/vacancies, and forming heterostructures can modulate the electronic structure, optimizing the adsorption/desorption of reactant intermediates and products [21]. This synergistic approach significantly enhances reactivity, resulting in superior ORR electrocatalytic performance. Therefore, incorporating the material onto a conductive carbon sphere surface enables effective dispersion of active Co metal sites, maximizing metal atom utilization and facilitating mass and electron transfer [22]. Thus, the integration of metal Co with MnO on NC represents an ideal strategy for enhancing ORR performance.

In this work, Co/MnO was successfully designed and synthesized through hydrothermal and pyrolytic methods, immobilized on NC carriers with abundant vacancies (Co/MnO@NC). The collaboration between the highly conductive metallic Co and defective MnO promotes swift electron transfer and improves the adsorption of oxygen reactants. The large specific surface area exposes more active sites, while the mesoporous structure promotes efficient mass and electron transfer. Consequently, the Co/MnO@NC catalyst exhibits outstanding electrocatalytic performance in ORR. The Co/MnO@NC-based liquid/solid-state ZABs achieved an impressive power density of 217.7 and 63.3 mW cm^{-2}, along with exceptional durability lasting approximately 459 h without significant degradation.

2. Experimental section

2.1. Chemicals and reagents

Cobalt (II) nitrate hexahydrate ($Co(NO_3)_2{\cdot}6H_2O$, ≥99.0 %), Manganese (II) chloride tetrahydrate ($MnCl_2{\cdot}4H_2O$, ≥99.0 %), Glucose ($C_6H_{12}O_6$,$\cdot 6H_2O$, specific spectral index = +52.5°~53.0°). Absolute ethanol (C_2H_5OH, 99.7 %) were sourced from xilong chemical Co., Ltd. Zinc acetate ($Zn(Ac)_2$, 99.0 %), and commercial Pt/C (20 wt% Pt) were acquired from Shanghai Aladdin Biochemical Technology Co., Ltd. Potassium hydroxide (KOH, 95 %) was obtained from Macklin Biochemical Co., Ltd. Nafion (5 % solution) was procured from Alfa Aesar. All reagents were analytical grade and were utilized without further purification. The RuO_2 powder was prepared by calcining $RuCl_3{\cdot}xH_2O$ (99 %, Ru 37 ~ 40 %) in air at 400 °C.

2.2. Synthesis of carbon spheres (Cs)

Carbon spheres (Cs) were prepared following a previously reported method [23]. Initially, 25 μL of 1 M KOH was introduced into 40 mL of 0.5 M glucose solution with vigorous stirring. The mixture was then transferred to a Teflon-lined stainless steel autoclave and kept at 180 °C for 6 h. Subsequently, the solution underwent centrifugation for extraction. The obtained product was washed several times with deionized water and ethanol, followed by drying overnight at 60 °C.

2.3. Synthesis of CoMn precursor

In a typical synthesis, 2 mmol $Co(NO_3)_2{\cdot}6H_2O$, 2 mmol $MnCl_2{\cdot}4H_2O$, 0.5 g of prepared glucose carbon spheres, and 3.6 g of urea were dissolved in a solution consisting of 30 mL of isopropyl alcohol and 6 mL of deionized water. After thorough stirring, the mixture was transferred to a Teflon-line stainless steel autoclave and maintained at 120 °C for 6 h. After naturally cooling to room temperature, the sample was centrifuged and subsequently dried at 80 °C.

2.4. Synthesis of Co/MnO@NC

The resulting CoMn precursor sample was finely ground with a certain amount of dicyanodiamine. Subsequently, the mixture was subjected to a temperature of 1000 °C for 2 h in a tube furnace under a protective N_2 atmosphere.

In addition, to finely tune the Co/Mn ratio while maintaining a constant total substance amount of 4 mmol, the ratios of Co/Mn were varied as 0:4, 1:3, 1:1, 3:1, and 4:0.

2.5. Synthesis of Cs@NC

Cs@NC was synthesized following a comparable approach to Co/MnO@NC, with the exception of substituting the CoMn precursor with Cs.

3. Results and discussion

3.1. Synthesis and structural analysis

In Fig. 1a, the sequential synthesis of Co/MnO@NC is illustrated. Initially, glucose carbon spheres were prepared according to our prior work. The X-ray diffraction (XRD) analysis of the prepared Cs unveiled two distinctive carbon peaks [24,25], validating the successful synthesis of Cs (Fig. S2a). Subsequently, CoMn species were synthetized on the Cs through a hydrothermal method, followed by a high-temperature pyrolysis process (1000 °C) using dicyandiamide as the nitrogen source. This results in a distinctive Co/MnO composite material stabilized on a NC matrix (Co/MnO@NC) during high-temperature calcination. This can be attributed to the reduction of high-valence cobalt to metallic cobalt at elevated temperatures, while the strongly oxidizing Mn^{2+} retains its higher valence state [26]. The metal molar ratio and pyrolysis temperature were meticulously adjusted to achieve the optimal ORR catalyst. The crystal structures of the catalysts were analyzed using XRD, as depicted in Fig. 1b and Fig. S3. The main peaks of Co at 44.0°, 51.2°, and 75.6° align well with Co (JCPDS: 15–0806) [27], and the rest match perfectly to MnO (JCPDS: 71–1177) [28] except for the C peak at 26.0°

[29]. Furthermore, the RuO_2 powder obtained through air calcination aligns with the standard tetragonal RuO_2 (JCPDS: 40–1290) as depicted in Fig. S4a. Additionally, it exhibits a nanoparticle morphology, as illustrated in Fig. S4b. Raman spectroscopy identified the presence of Co-Co dominant vibrational modes in Co@NC and Co/MnO@NC samples at 193, 476, and 688 cm^{-1}, respectively (Fig. 1c) [30]. The D-band (defective carbon) and G-band (graphitized carbon) were observed at 1316 and 1590 cm^{-1}, respectively. The peak intensity ratios (I_D/I_G) reflect the degree of defects and graphitization of the carbon-based catalysts [31]. Catalysts synthesized using a CoMn molar ratio of 3/1 and calcined at 1000 °C exhibited a higher I_D/I_G (Fig. S5), indicating a greater abundance of carbon edge defects and enhanced electrocatalytic activity [32]. Furthermore, Co/MnO@NC showed a higher I_D/I_G value (1.98) compared to Co@NC (1.55) and MnO@NC (1.77), indicating that metal Co significantly improves the electrical conductivity of Co/MnO@NC. The presence of MnO-coupled Co creates more defective sites, promoting the adsorption of oxygen and other reaction intermediates in the ORR process [33]. Additionally, a Raman band at 2614 cm^{-1} corresponding to 2D carbon was observed in all samples [30]. Electron paramagnetic resonance (EPR) spectroscopy was employed to confirm the formation of defects (Fig. 1d). The appearance of a broad signal attributable to the contribution of unpaired electrons, unequivocally verified the existence of defects [34]. Intriguingly, Co@NC and Co/MnO@NC are significantly negatively shifted compared to MnO@NC, signifying the likelihood of combined oxygen vacancies and metal defects in the coupled Co and MnO configuration. This facilitates the increase in inherent conductivity within Co/MnO@NC, while simultaneously enhancing the dissociation of O_2 by elongating the O—O bond [35,36]. The Brunauer-Emmett-Teller (BET) specific surface area and pore size distributions of the synthesized catalysts were obtained from the N_2 adsorption–desorption isotherms (Fig. 1e and Fig. S6). Co/MnO@NC, MnO@NC, and Co@NC all exhibited type IV isotherms with hysteresis loops[29]. Furthermore, the BET of Co/MnO@NC (151.13 $m^2\ g^{-1}$) was higher than that of MnO@NC (121.39 $m^2\ g^{-1}$), and slightly lower than that of Co@NC (157.08 $m^2\ g^{-1}$), indicating that Co/MnO@NC possesses a large specific surface area and a mesoporous structure conducive to mass and electron transfer in the electrocatalytic process [37].

The structural morphology of the prepared samples was investigated through scanning electron microscopy (SEM) and transmission electron microscopy (TEM). The synthesized Cs exhibited a spherical morphology with a sleek surface (Fig. S2b). In comparison to the Cs precursor, the surface of Co/MnO@NC became relatively rough while maintaining the original spherical morphology (Fig. 2a). The TEM image further revealed Co/MnO loaded in the carbon matrix nanospheres (Fig. 2b). High-resolution TEM images (Fig. 2c) displayed the lattice spacing of 0.281 nm corresponding to the (2 0 0) crystal plane of MnO and 0.212 nm corresponding to the (1 1 1) crystal plane of Co. Notably, circled in blue dashed lines is the (0 0 2) defective crystal plane of C outside the Co/MnO rim, indicating the presence of an *N*-doped carbon shell. High-angle annular dark-field scanning TEM (HAADF-STEM) and elemental mapping showed a uniform elemental distribution of Co, Mn, O, C, and N (Fig. 2d), affirming the successful construction of MnO/Co@NC. Meanwhile, energy dispersive X-ray spectroscopy (EDS) analysis further confirmed the presence of Co, Mn, O, N, and C elements, as illustrated in Fig. S7. Additionally, inductively coupled plasma mass spectrometry (ICP-MS) was utilized to accurately measure the metal element content of Co/Mn in the prepared catalysts (Table S1). The contact angle serves as a crucial parameter in evaluating the wetting properties of solid surfaces, where a contact angle (θ) below 90° between the solid–liquid and gas–liquid interfaces indicates a hydrophilic surface [38]. Remarkably, the Co/MnO@NC catalyst displayed a contact angle of 72.87°, in stark contrast to the contact angles of MnO@NC (132.68°) and Co@NC (116.93°) in Fig. 2e. These results indicate that the coupling of Co and MnO creates a more hydrophilic surface, enabling enhanced wetting by liquids containing dissolved oxygen, thus promoting the ORR at the interface [39,40].

The elemental composition and surface chemical state of the synthesized catalysts were examined using X-ray photoelectron spectroscopy (XPS). The XPS full spectrum (Fig. S8) unequivocally showcased the existence of Co, Mn, O, C, and N elements. The high-resolution C1s spectrum of Co/MnO@NC unveiled four distinct peaks (Fig. S9), meticulously aligned with the C═C (284.0 eV), C—C (284.8 eV), C—O (286.0 eV), and C═O bonds (289.6 eV), respectively [41]. The deconvolution of Co 2*p* XPS spectra of Co/MnO@NC and Co@NC (Fig. 3a) can be divided into two double peaks, Co $2p_{1/2}$ (794.2 eV: Co^0 and satellite peaks) and Co $2p_{3/2}$ (778.5 eV: Co^0 and satellite peaks). Importantly, the presence of a low-valent Co^0 site plays a crucial role in fortifying the stability of the Mn-O bond, ensuring its integrity. Moreover, the Mn 2*p* XPS spectroscopy results demonstrated that the majority of Mn species in the Co/MnO@NC and MnO@NC were Mn(II), with accompanying satellite peaks (Fig. 3b) [26]. The high-resolution O 1 *s* spectra were divided into three peaks (Fig. 3c) for metal–oxygen (O_L), oxygen vacancies (O_V)/carbon–oxygen bond (O-C═O), and surface adsorbed

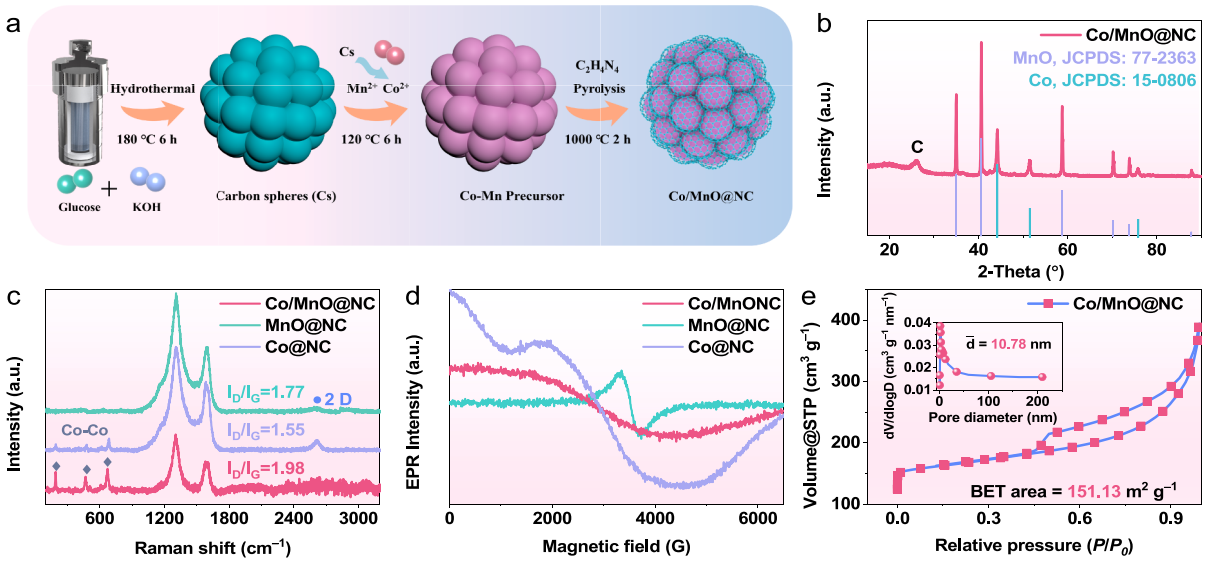

Fig. 1. (a) Schematic illustration of the synthesis of Co/MnO@NC. (b) XRD pattern of Co/MnO@NC. (c) Raman spectra, (d) the EPR spectra of the as-prepared catalysts, and (e) N_2 adsorption–desorption isotherm of Co/MnO@NC (inset: corresponding pore size distribution curve).

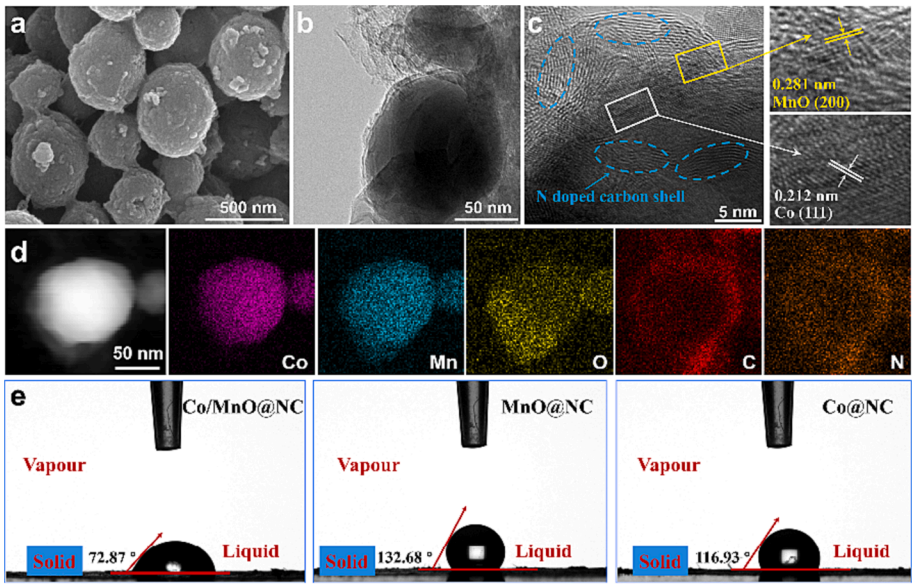

Fig. 2. (a) SEM image, (b) TEM image, (c) HR-TEM image, and (d) HAADF-STEM images and the corresponding elemental mappings of Co/MnO@NC. (e) Contact angle measurements of Co/MnO@NC, MnO@NC and Co@NC.

oxygen (O_A) at 530.2, 532.1, and 533.9 eV, respectively [42]. In Fig. 3d, the high-resolution XPS spectra of N 1 *s* depict distinct peaks corresponding to pyridine nitrogen (398.5 eV), pyrrole nitrogen (400.5 eV), graphitic nitrogen (401.3 eV), and nitrogen oxide (404.2 eV) [43]. Remarkably, the Co/MnO@NC presented the highest proportion of pyridine nitrogen, accounting for 42.30 % (Table S2). The presence of abundant pyridine nitrogen significantly contributes to the catalytic promotion of the ORR [44].

3.2. ORR activity in alkaline media

The electrocatalysts' ORR electrocatalytic activity was assessed in 0.1 M KOH to investigate the impact of varying metal ratios and calcination temperatures on catalytic performance (Figs. S10-11). Remarkably, the results unveiled that a Co/Mn ratio of 3/1 exhibited optimal performance, with the highest activity achieved at a calcination temperature of 1000 °C. In Fig. 4a, Co/MnO@NC displayed higher cathodic peak positions than Co@NC, MnO@NC, and Pt/C, indicating superior ORR activity. Furthermore, Co/MnO@NC exhibited outstanding ORR performance, outperforming Co@NC, MnO@NC, Cs@NC, and even rivalling Pt/C. It achieved a half-wave potential ($E_{1/2}$) of 0.80 V and a limiting current density (j_L) of 5.1 mA cm^{-2}, as illustrated in Fig. 4b and Fig. S12. The Tafel slope is a reliable indicator of ORR reaction kinetics, certified superior reaction kinetics for Co/MnO@NC [45–47], with a Tafel slope of 67 mV dec^{-1}, significantly lower than that of MnO@NC (109 mV dec^{-1}), Co@NC (80 mV dec^{-1}), and Pt/C (88 mV dec^{-1}), as depicted in Fig. 4c. Moreover, a comprehensive comparison was undertaken for the obtained three catalysts, affirming the profound enhancement of ORR performance in MnO achieved through the strategic coupling with Co (Fig. 4d and Table S3). Moreover, the Co/MnO@NC catalyst demonstrated exceptional superiority compared to the majority of recently reported catalysts (Table S4).

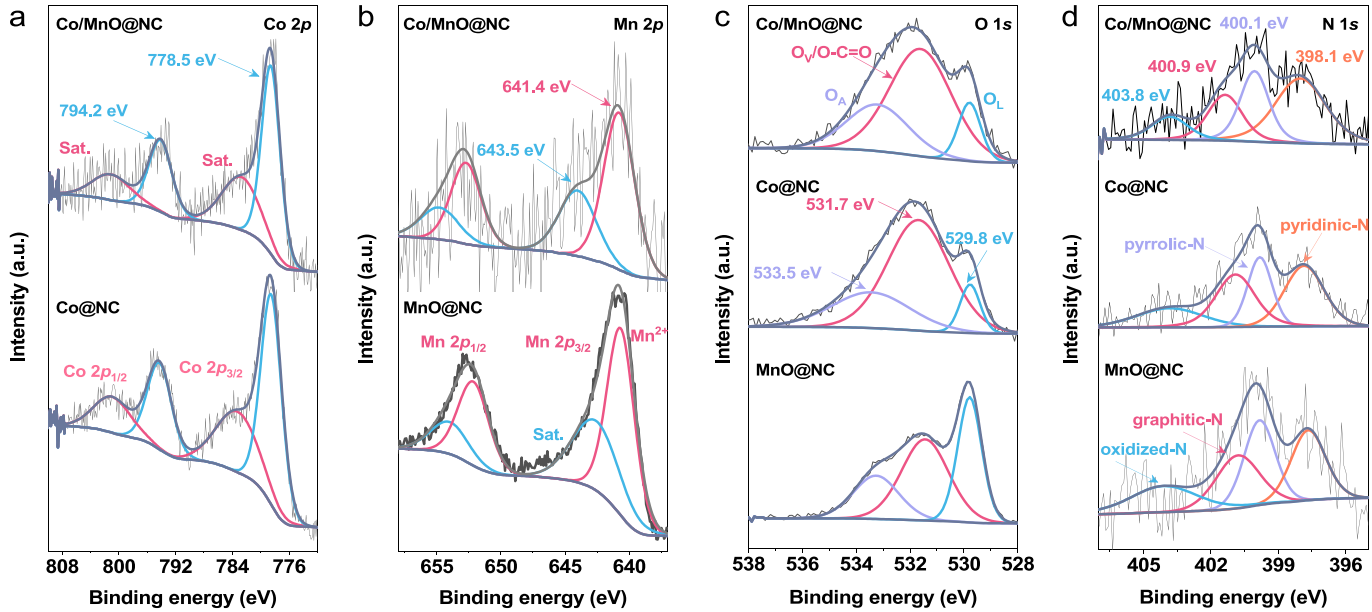

Fig. 3. High-resolution XPS spectra of (a) Co 2*p*, (b) Mn 4*f*, (c) O 1 *s*, and (d) N 1 *s* in as-synthesized samples.

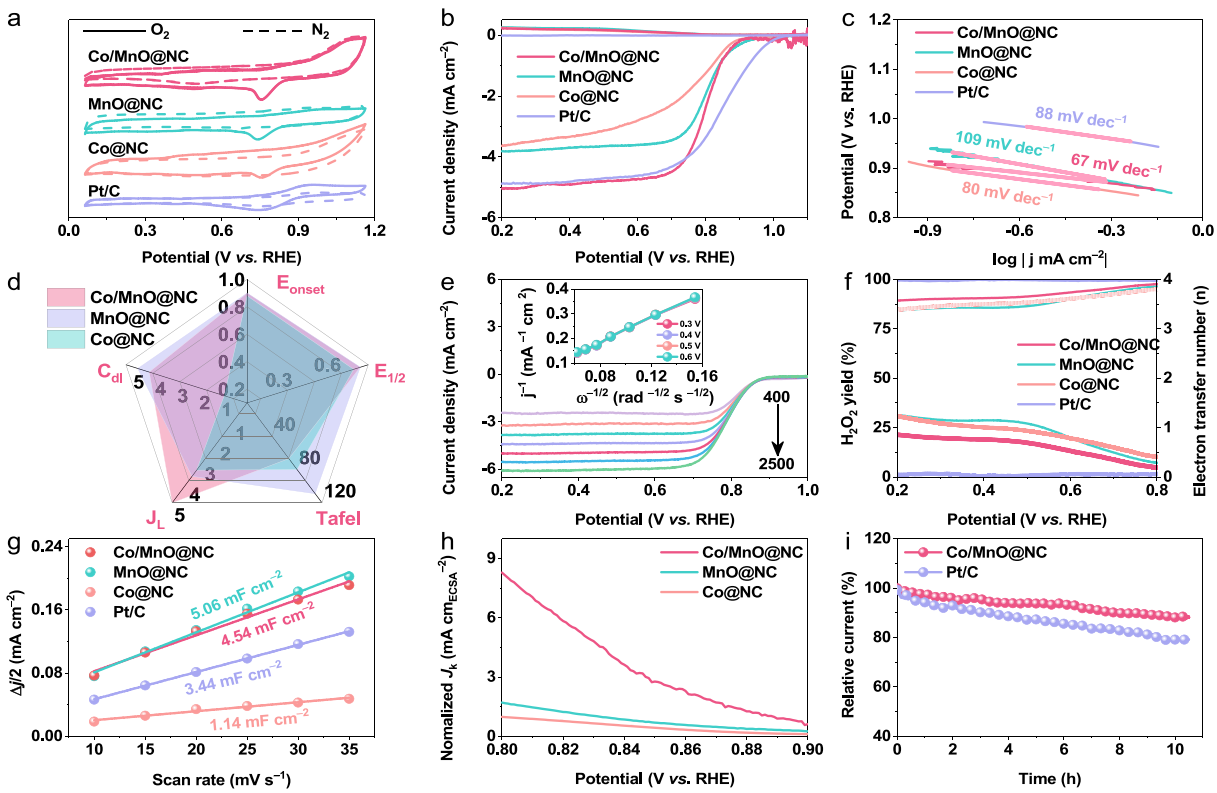

Fig. 4. Electrochemical performance of different catalysts. (a) CV curves in N_2 or O_2-saturated 0.1 M KOH solution. (b) LSV polarization curves in O_2-saturated 0.1 M KOH electrolyte, (c) Tafel plots, (d) the corresponding initial potential (E_{onset}), half-wave potential ($E_{1/2}$), Tafel, limiting current density (J_L), and double layer capacitance (C_{dl}). (e) Polarization curves of Co/MnO@NC with various rotating speeds from 400 to 2500 rpm. (f) The corresponding K-L plots. (g) H_2O_2 yield (%) and electron transfer number (n) from various catalysts. (h) C_{dl} values. (i) The corresponding stability test in O_2-saturated 0.1 M KOH solution at a rotating speed of 1600 rpm.

In addition, Co/MnO@NC underwent ORR polarization curve tests at different rotation speeds within the range of 400–1600 rpm (Fig. 4e), exhibiting a gradual surge in the diffusion-limited current with an increase in rotation speed. The Koutechy-Levich (K-L) diagram (Fig. 4f) further confirmed its electron transfer number (n) to be nearly 4, supporting the notion that the reaction is a highly efficient four-electron transfer process [48]. The results depicted in Fig. 4g simultaneously highlight the exceptional selectivity of Co/MnO@NC for the direct four-electron ($4e^-$) reduction pathway, as indicated by the low H_2O_2 yield and high electron transfer number (>3.9), underscoring the superior ORR performance of Co/MnO@NC. To explore the electrochemically active surface area (ECSA), we conducted CV measurements in the non-redox region (Fig. S13). The Co/MnO@NC catalyst exhibited an electrochemical double-layer capacitance (C_{dl}) of 4.54 mF cm^{-2}, surpassing that of the Co@NC (1.14 mF cm^{-2}) and Pt/C (3.44 mF cm^{-2}) catalysts, while falling slightly lower than the MnO@NC (5.06 mF cm^{-2}). Furthermore, CV measurements were conducted using $K_3[Fe(CN)_6]$ to assess the ECSA of the synthesized catalysts (Fig. S14). As anticipated, the Co/MnO@NC exhibited the highest slope of 52.5 (Fig. S15). Typically, a greater ECSA results (Fig. S16) in an expanded electrode–electrolyte interface area, effectively uncovering more active sites [49]. To further substantiate this, we standardized the kinetic current density (J_k). The results clearly indicate the superior performance of Co/MnO@NC in terms of normalized J_k (Fig. 4h), surpassing both Co@NC and MnO@NC. This underscores the presence of a larger number of catalytically efficient active sites within Co/MnO@NC [50]. Furthermore, to assess the methanol tolerance of Co/MnO@NC and Pt/C catalysts, we conducted chronoamperometric tests in O_2-saturated 0.1 M KOH solution at 1600 rpm. Remarkably, the cathodic current of Co/MnO@NC exhibited negligible fluctuation upon the introduction of methanol, whereas the commercial Pt/C experienced a significant decrease (Fig. S17). This observation highlighted the exceptional methanol tolerance of Co/MnO@NC. This suggests its promising suitability for practical applications in direct methanol fuel cells and metal-air batteries. A long-term chronoamperometric test was conducted to evaluate the durability of the catalysts. The Co/MnO@NC displayed remarkable stability even after 10 h of continuous operation, in contrast to Pt/C, underscoring the superior durability of Co/MnO@NC (Fig. 4).

3.3. Test for performance of assembled ZABs

In light of the remarkable electrocatalytic performance displayed by Co/MnO@NC, we proceeded to assemble an aqueous ZAB to evaluate its promising applications in energy storage and conversion systems. Considering the less-than-impressive oxygen evolution reaction (OER) performance (354 mV@10 mA cm^{-2}) of Co/MnO@NC in Fig. S18, we conducted a charge–discharge stability test of the ZAB using Co/MnO@NC + RuO_2 (mass ratio = 2:1) as the air cathode. Simultaneously, a Pt/C + RuO_2 catalyst was prepared for comparative analysis. Fig. 5a illustrates the schematic diagram of the ZAB configuration, with a meticulously polished zinc plate serving as the anode, Co/MnO@NC as the cathode, and the electrolyte comprising a 6.0 M KOH solution containing 0.2 M $Zn(AC)_2$. As depicted in Fig. 5b, the Co/MnO@NC-based ZAB displayed a commendable open-circuit voltage (OCV) of 1.47 V, surpassing that of the Pt/C-based ZAB (1.42 V). Impressively, the Co/MnO@NC-based ZAB achieved a remarkable peak power density of 217.7 mW cm^{-2} (Fig. 5c), showcasing a 1.74-fold enhancement over the Pt/C-based ZAB (127.6 mW cm^{-2}). Moreover, the Co/MnO@NC-based ZAB demonstrated a sufficient voltage output, capable of illuminating an LED (~3.0 V), as indicated in Fig. S19. Significantly, a rigorous long-term stability test was conducted at a current density of 5 mA cm^{-2} (Fig. 5d). Impressively, the Co/MnO@NC-based ZAB showcased

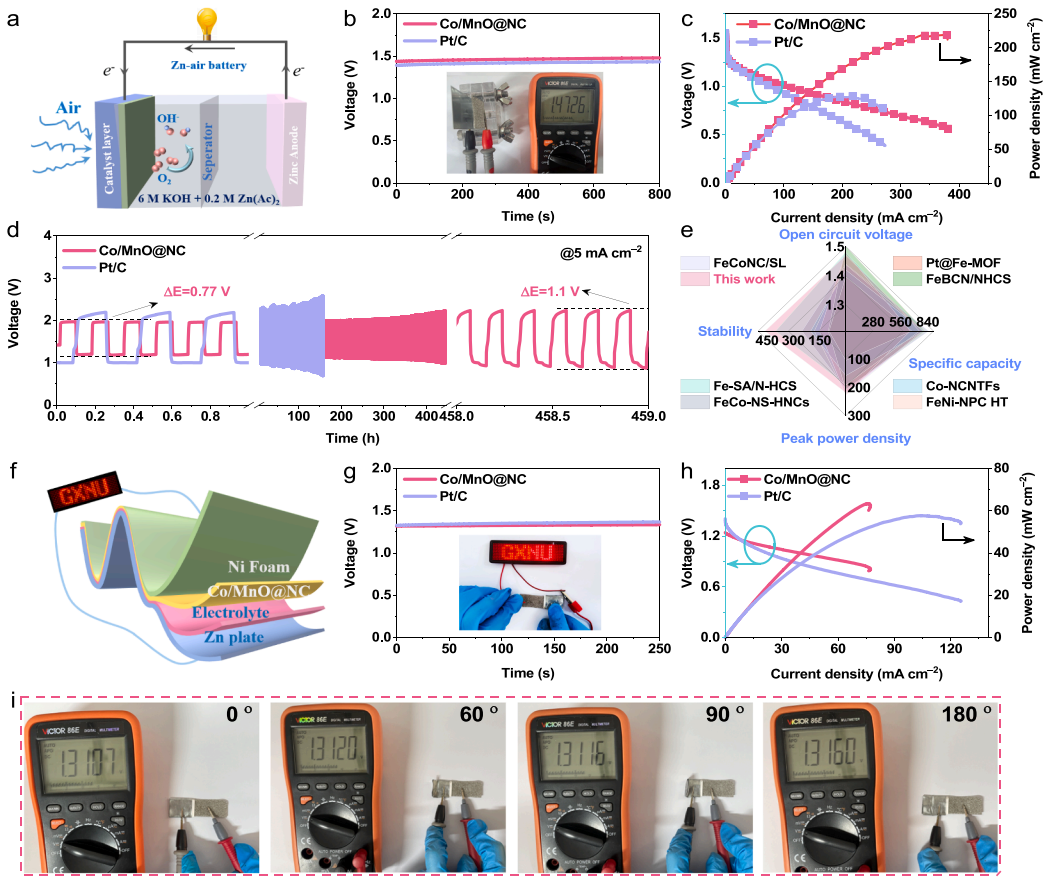

Fig. 5. (a) Schematic configuration of assembled aqueous ZAB. (b) OCV of the ZABs. (c) Discharge polarization curves and the corresponding power densities of the ZABs. (d) Comparison of Co/MnO@NC as air cathode with other recently reported excellent catalysts. (e) Galvanostatic cycling at 5 mA cm^{-2} (20 min for each cycle). (f) Sketch diagram of the flexible ZAB. (g) OCVs of Co/MnO@NC and Pt/C-based flexible ZABs (inset: Co/MnO@NC-based flexible ZAB-lit LED board). (h) The discharge polarization and corresponding power density profiles of the flexible ZABs. (i) OCVs at different bending angles of Co/MnO@NC-based flexible ZAB powered by LED panel at different bending angles.

remarkable stability, with a negligible voltage gap decay of only 0.33 V after continuous operation for 459 h. In stark contrast, the Pt/C-based ZAB suffered significant attenuation within a mere 157 h, underscoring the robustness of Co/MnO@NC. Satisfyingly, Co/MnO@NC demonstrated significant advantages in OCV, specific capacity, power density and stability based on the recently reported performance of ORR catalysts for ZAB (Fig. 5e and Table S5), offering promising prospects for its practical application. Due to the remarkable performance of Co/MnO@NC, a flexible ZAB was delicately designed. The solid ZAB was assembled using a carbon cloth coated with Co/MnO@NC as the air cathode, a zinc foil as the anode, and a polyvinyl alcohol (PVA) hydrogel as the solid electrolyte (Fig. 5f). Crucially, the incorporation of a layer of weighing paper between the zinc foil and nickel foam acts as a protective barrier, efficiently averting any possible short-circuiting in the solid battery. As depicted in Fig. 5g, the Co/MnO@NC-based solid-state battery exhibited an impressive OCV of 1.36 V, surpassing the Pt/C-based solid-state ZAB (1.33 V). Moreover, the Co/MnO@NC-based flexible battery showcased its remarkable capability by successfully powering a "GXNU" LED board (inset of Fig. 5g). Even more noteworthy, the Co/MnO@NC-ZAB demonstrated a peak power density of 63.3 mW cm^{-2} (Fig. 5h), senior to Pt/C-ZAB (57.5 mW cm^{-2}) and most recently reported catalysts (Table S6), demonstrating its tremendous potential in practical applications. The Co/MnO@NC-based flexible ZAB impeccably exhibits its flexibility and stability, as eloquently demonstrated by the steady voltage measurements captured at various bending angles (0°, 60°, 90°, 180°), as depicted in Fig. 5i.

The Co/MnO@NC catalyst exhibits an ORR mechanism driven by several synergistic effects. Firstly, the incorporation of metal Co enhanced the electrical conductivity of the catalyst, thereby facilitating electron transfer. The presence of MnO promotes the adsorption of oxygen-containing intermediates, effectively lowering the reaction energy barrier [51]. Additionally, the tailored vacancies can effectively adjust the electronic configuration and enhance the binding affinity with oxygen intermediates, thus improving ORR catalytic activity [52]. Superhydrophilicity plays a crucial role in enhancing active site-reactant interaction and expediting ORR kinetics. Moreover, the NC component plays a critical role in protecting the active site, enhancing catalyst stability [53], and synergistically amplifying ORR kinetics in collaboration with Co and MnO. Specifically, Fig. S20 provides further insight into the proposed ORR process. Initially, O_2 molecules are adsorbed on the active sites (metal Co and Mn^{2+}) of Co/MnO@NC surface. Subsequently, the O—O bonds undergo cleavage, resulting in the formation of the oxygen intermediate *OOH and *O. Ultimately, *O undergoes protonation to generate OH^- [54,55].

4. Conclusions

We have successfully synthesized a high-performance Co/MnO@NC oxygen reduction reaction (ORR) electrocatalyst with abundant vacancies using a high-temperature pyrolysis strategy. This spherical catalyst exhibits exceptional performance in both aqueous and solid-state zinc-air batteries (ZABs), achieving peak power densities of 217.7 and 63.3 mW cm^{-2}, respectively. Remarkably, it demonstrates exceptional stability in an aqueous ZAB for an impressive 459 h, even maintaining voltage stability under external mechanical stress in a solid-state ZAB. The Co/MnO@NC catalyst's outstanding performance stems

from several key factors. Metallic Co boosts electrical conductivity, while MnO enhances oxygenated intermediate adsorption. Abundant vacancies fine-tune the electronic configuration, optimizing activity. Additionally, the superhydrophilic surface ensures optimal electrolyte contact and the *N*-doped carbon framework stabilizes the active sites, contributing significantly to overall stability. This work paves the way for developing highly active and stable ORR electrocatalysts for practical energy conversion applications.

CRediT authorship contribution statement

Lixia Wang: Writing – original draft. **Jia Huang:** Methodology, Investigation. **Xinran Hu:** Methodology. **Zhiyang Huang:** Supervision, Methodology. **Mingcheng Gao:** Data curation. **Di Yao:** Writing – review & editing. **Tayirjan Taylor Isimjan:** Writing – review & editing, Conceptualization. **Xiulin Yang:** Writing – review & editing, Project administration.

Declaration of competing interest

The authors declare that they have no known competing financial interests or personal relationships that could have appeared to influence the work reported in this paper.

Data availability

Data will be made available on request.

Acknowledgements

This work has been supported by the National Natural Science Foundation of China (no. 21965005, 52363028), Natural Science Foundation of Guangxi Province (2021GXNSFAA076001), Guangxi Technology Base and Talent Subject (GUIKE AD18126001, GUIKE AD20297039), and Innovation Project of Guangxi Graduate Education (YCBZ2023056).

Appendix A. Supplementary material

Supplementary data to this article can be found online at https://doi.org/10.1016/j.jcis.2024.01.143.

References

[1] J.-C. Wu, X.-C. Shen, H. Wang, D.-J. Deng, S.-Q. Wu, Y. Gong, L.-H. Zhu, L. Xu, H.-N. Li, Electronic structure modification of $FeWO_4$ through F doping for enhanced oxygen reduction performance in zinc–air batteries, Mater. Today Phys. 38 (2023) 101274, https://doi.org/10.1016/j.mtphys.2023.101274.

[2] X. Li, C. Li, Y. Xie, S. Pan, F. Luo, Z. Yang, Anion effect on oxygen reduction reaction activity of nitrogen doped carbon nanotube encapsulated cobalt nanoparticles, Appl. Surf. Sci. 648 (2024) 158975, https://doi.org/10.1016/j.apsusc.2023.158975.

[3] Z. Nie, L. Zhang, Q. Zhu, Z. Ke, Y. Zhou, T. Wågberg, G. Hu, Reversed charge transfer induced by nickel in Fe-Ni/Mo_2C@nitrogen-doped carbon nanobox for promoted reversible oxygen electrocatalysis, J. Energy Chem. 88 (2024) 202–212, https://doi.org/10.1016/j.jechem.2023.09.009.

[4] X. Wang, L. Xu, C. Zhou, N.H. Wong, J. Sunarso, R. Ran, W. Zhou, Z. Shao, Toward self-supported bifunctional air electrodes for flexible solid-state Zn–air batteries, Small Sci. 3 (2023) 2300066, https://doi.org/10.1002/smsc.202300066.

[5] D. Deng, H. Zhang, J. Wu, X. Tang, M. Ling, S. Dong, L. Xu, H. Li, H. Li, Electronic structure and spin state regulation of vanadium nitride via a sulfur doping strategy toward flexible zinc-air batteries, J. Energy Chem. 89 (2024) 239–249, https://doi.org/10.1016/j.jechem.2023.10.024.

[6] D. Deng, J. Qian, X. Liu, H. Li, D. Su, H. Li, H. Li, L. Xu, Non-covalent interaction of atomically dispersed Cu and Zn pair sites for efficient oxygen reduction reaction, Adv. Funct. Mater. 32 (2022) 2203471, https://doi.org/10.1002/adfm.202203471.

[7] L. Yang, Y. Zhu, X. Yao, C. Du, Z. Han, J. Tian, X. Liu, X. Ma, C. Cao, Surface-optimized carbon nanocages with tailorable atomic Fe-N_4 sites to boost oxygen reduction in long stable zinc-air battery, Energy Storage Mater. 63 (2023) 102972, https://doi.org/10.1016/j.ensm.2023.102972.

[8] D.D. Chen Pu, Henan Li, Li Xu, $Fe_{0.64}Ni_{0.36}$@Fe_3NiN Core-Shell Nanostructure Encapsulated in N-Doped Carbon Nanotubes for Rechargeable Zinc-Air Batteries with Ultralong Cycle Stability, Acta Phys. -Chim. Sin., 40 (2024) 2304021, 10.3866/pku.whxb202304021.

[9] Z. Lin, O. Sheng, X. Cai, D. Duan, K. Yue, J. Nai, Y. Wang, T. Liu, X. Tao, Y. Liu, Solid polymer electrolytes in all-solid-state lithium metal batteries: From microstructures to properties, J. Energy Chem. 81 (2023) 358–378, https://doi.org/10.1016/j.jechem.2023.01.063.

[10] F. Luo, S. Pan, Y. Xie, C. Li, Y. Yu, Z. Yang, Atomically dispersed Ni electrocatalyst for superior urea-assisted water splitting, J. Energy Chem. 90 (2024) 1–6, https://doi.org/10.1016/j.jechem.2023.10.007.

[11] H. Zheng, F. Ma, H. Yang, X. Wu, R. Wang, D. Jia, Z. Wang, N. Lu, F. Ran, S. Peng, Mn, N co-doped Co nanoparticles/porous carbon as air cathode for highly efficient rechargeable Zn-air batteries, Nano Res. 15 (2022) 1942–1948, https://doi.org/10.1007/s12274-021-3837-6.

[12] Y. Zhao, B. Li, Y. Li, X. Fan, F. Zhang, G. Zhang, Q. Xia, W. Peng, Synergistic activation of peroxymonosulfate between Co and MnO for bisphenol A degradation with enhanced activity and stability, J. Colloid Interface Sci. 623 (2022) 775–786, https://doi.org/10.1016/j.jcis.2022.05.105.

[13] Q. Zhou, S. Hou, Y. Cheng, R. Sun, W. Shen, R. Tian, J. Yang, H. Pang, L. Xu, K. Huang, Y. Tang, Interfacial engineering Co and MnO within N, S co-doped carbon hierarchical branched superstructures toward high-efficiency electrocatalytic oxygen reduction for robust Zn-air batteries, Appl. Catal. B Environ. 295 (2021) 120281, https://doi.org/10.1016/j.apcatb.2021.120281.

[14] X.F. Lu, Y. Chen, S. Wang, S. Gao, X.W. Lou, Interfacing manganese oxide and cobalt in porous graphitic carbon polyhedrons boosts oxygen electrocatalysis for Zn–air batteries, Adv. Mater. 31 (2019) 1902339, https://doi.org/10.1002/adma.201902339.

[15] H. Xia, R. Pang, X. Dong, Q. Liu, J. Chen, E. Wang, J. Li, Boosting oxygen reduction reaction kinetics by designing rich vacancy coupling pentagons in the defective carbon, J. Am. Chem. Soc. 145 (2023) 25695–25704, https://doi.org/10.1021/jacs.3c08556.

[16] S. Chen, Y. Ma, L. Zhang, Y. Zhang, Y. Chen, X. Zhang, J. Yan, The contact interface electronic coupling of cobalt and zirconia enables stable and highly efficient $4e^-$ oxygen reduction reaction catalysis, Small (2023) 2307278, https://doi.org/10.1002/smll.202307278.

[17] H. Liu, S. Zhu, Z. Cui, Z. Li, S. Wu, Y. Liang, Unveiling the roles of multiple active sites during oxygen reduction reaction in Cr_2O_3@Cr-N-C composite catalyst, J. Catal. 396 (2021) 402–408, https://doi.org/10.1016/j.jcat.2021.03.015.

[18] G. Wang, M. Zhang, G. Zhang, Z. Wang, X. Chen, X. Ke, C. Wang, S. Chu, M. Sui, Novel approach of diffusion-controlled sequential reduction to synthesize dual-atomic-site alloy for enhanced bifunctional electrocatalysis in acidic and alkaline media, Adv. Funct. Mater. (2023) 2308876, https://doi.org/10.1002/adfm.202308876.

[19] L. Wang, H. Yu, Z. Huang, Z. Luo, T.T. Isimja, S. Xu, X. Yang, Interface engineering of porous nickel-iron phosphates with enriched oxygen vacancies as an efficient bifunctional electrocatalyst for high current water splitting, Electrochim. Acta 443 (2023) 141932, https://doi.org/10.1016/j.electacta.2023.141932.

[20] A.G. Ramu, M.L.A. Kumari, M.S. Elshikh, H.H. Alkhamis, A.F. Alrefaei, D. Choi, A facile and green synthesis of CuO/NiO nanoparticles and their removal activity of toxic nitro compounds in aqueous medium, Chemosphere 271 (2021) 129475, https://doi.org/10.1016/j.chemosphere.2020.129475.

[21] H. Li, C. Zhang, W. Xiang, M.A. Amin, J. Na, S. Wang, J. Yu, Y. Yamauchi, Efficient electrocatalysis for oxygen evolution: W-doped NiFe nanosheets with oxygen vacancies constructed by facile electrodeposition and corrosion, Chem. Eng. J. 452 (2023) 139104, https://doi.org/10.1016/j.cej.2022.139104.

[22] Z. Huang, Y. Yao, Z. Pang, Y. Yuan, T. Li, K. He, X. Hu, J. Cheng, W. Yao, Y. Liu, A. Nie, S. Sharifi-Asl, M. Cheng, B. Song, K. Amine, J. Lu, T. Li, L. Hu, R. Shahbazian-Yassar, Direct observation of the formation and stabilization of metallic nanoparticles on carbon supports, Nat. Commun. 11 (2020) 6373, https://doi.org/10.1038/s41467-020-20084-5.

[23] J. Gao, G. Wang, W. Wang, L. Yu, B. Peng, A. El-Harairy, J. Li, G. Zhang, Engineering electronic transfer dynamics and ion adsorption capability in dual-doped carbon for high-energy potassium ion hybrid capacitors, ACS Nano 16 (2022) 6255–6265, https://doi.org/10.1021/acsnano.2c00140.

[24] S. Pan, C. Li, T. Xiong, Y. Xie, F. Luo, Z. Yang, Hydrogen spillover in MoOxRh hierarchical nanosheets boosts alkaline HER catalytic activity, Appl. Catal. B: Environ. 341 (2024) 123275, https://doi.org/10.1016/j.apcatb.2023.123275.

[25] F. Luo, S. Pan, Y. Xie, C. Li, Y. Yu, H. Bao, Z. Yang, Hydrazine-assisted acidic water splitting driven by iridium single atoms, Adv. Sci. 10 (2023) 2305058, https://doi.org/10.1002/advs.202305058.

[26] K. Li, R. Cheng, Q. Xue, T. Zhao, F. Wang, C. Fu, Construction of a Co/MnO Mott-Schottky heterostructure to achieve interfacial synergy in the oxygen reduction reaction for aluminum-air batteries, ACS Appl. Mater. Interfaces 15 (2023) 9150–9159, https://doi.org/10.1021/acsami.2c13871.

[27] L. Gu, Y. Li, A.D. Chowdhury, Controllable synthesis of efficient and robust carbon-incorporated ruthenium–cobalt mixed metal phosphide-based bifunctional electrocatalyst for the water and urea oxidation, Mater. Today Chem. 27 (2023) 101290, https://doi.org/10.1016/j.mtchem.2022.101290.

[28] Y. Niu, X. Teng, S. Gong, X. Liu, M. Xu, Z. Chen, Boosting oxygen electrocatalysis for flexible zinc-air batteries by interfacing iron group metals and manganese oxide in porous carbon nanowires, Energy Storage Mater. 43 (2021) 42–52, https://doi.org/10.1016/j.ensm.2021.08.037.

[29] C. Hu, Q. Liang, Y. Yang, Q. Peng, Z. Luo, J. Dong, T.T. Isimjan, X. Yang, Conductivity-enhanced porous N/P co-doped metal-free carbon significantly enhances oxygen reduction kinetics for aqueous/flexible zinc-air batteries,

J. Colloid Interface Sci. 633 (2023) 500–510, https://doi.org/10.1016/j.jcis.2022.11.118.
[30] W.-G. Cui, X.-Y. Zhuang, Y.-T. Li, H. Zhang, J.-J. Dai, L. Zhou, Z. Hu, T.-L. Hu, Engineering Co/MnO heterointerface inside porous graphitic carbon for boosting the low-temperature CO_2 methanation, Appl. Catal. B Environ. 287 (2021) 119959, https://doi.org/10.1016/j.apcatb.2021.119959.
[31] Z. Nie, M. Chen, L. Zhang, Q. Feng, J. Hu, X. Huang, C. Zhou, Y. Zhou, T. Wågberg, G. Hu, Tailoring the d-band center by intermetallic charge-transfer manipulation in bimetal alloy nanoparticle confined in N-doped carbon nanobox for efficient rechargeable Zn-air battery, Chem. Eng. J. 463 (2023) 142411, https://doi.org/10.1016/j.cej.2023.142411.
[32] M. Guo, Z. Huang, Y. Qu, L. Wang, H. Li, T.T. Isimjan, X. Yang, Synergistic effect and nanostructure engineering of three-dimensionally hollow mesoporous spherical Cu_3P/TiO_2 in aqueous/flexible Zn–air batteries, Appl. Catal. B Environ. 320 (2023) 121991, https://doi.org/10.1016/j.apcatb.2022.121991.
[33] L. Zhang, Y. Dong, L. Li, L. Wei, J. Su, L. Guo, Enhanced oxygen reduction activity and stability of double-layer nitrogen-doped carbon catalyst with abundant Fe-Co dual-atom sites, Nano Energy 117 (2023) 108854, https://doi.org/10.1016/j.nanoen.2023.108854.
[34] Y. Hu, M. Guo, C. Hu, J. Dong, P. Yan, T. Taylor Isimjan, X. Yang, Engineering cobalt nitride nanosheet arrays with rich nitrogen defects as a bifunctional robust oxygen electrocatalyst in rechargeable Zn–air batteries, J. Colloid Interface Sci. 608 (2022) 2066–2074, https://doi.org/10.1016/j.jcis.2021.10.128.
[35] Y. Go, K. Min, H. An, K. Kim, S. Eun Shim, S.-H. Baeck, Oxygen-vacancy-rich CoFe/$CoFe_2O_4$ embedded in N-doped hollow carbon spheres as a highly efficient bifunctional electrocatalyst for Zn–air batteries, Chem. Eng. J. 448 (2022) 137665, https://doi.org/10.1016/j.cej.2022.137665.
[36] D. Wang, Y.-P. Deng, Y. Zhang, Y. Zhao, G. Zhou, L. Shui, Y. Hu, M. Shakouri, X. Wang, Z. Chen, Defect engineering on three-dimensionally ordered macroporous phosphorus doped Co_3O_4–δ microspheres as an efficient bifunctional electrocatalyst for Zn-air batteries, Energy Storage Mater. 41 (2021) 427–435, https://doi.org/10.1016/j.ensm.2021.06.017.
[37] C. Xu, Y. Niu, S. Gong, X. Liu, M. Xu, T. Liu, Z. Chen, Integrating bimetal alloy into N-doped carbon nanotubes@nanowires superstructure for Zn-air batteries, ChemSusChem 15 (2022) e202200312, https://doi.org/10.1002/cssc.202200312.
[38] J.-W. Song, L.-W. Fan, Temperature dependence of the contact angle of water: A review of research progress, theoretical understanding, and implications for boiling heat transfer, Adv. Colloid Interface Sci. 288 (2021) 102339, https://doi.org/10.1016/j.cis.2020.102339.
[39] X. Meng, J. Xie, Y. Sun, J. Liu, B. Liu, R. Wang, F. Ma, M. Liu, J. Zou, Fe_2O_3/spinel $NiFe_2O_4$ heterojunctions in-situ wrapped by one-dimensional porous carbon nanofibers for boosting oxygen evolution/reduction reactions, Int. J. Hydrogen Energy 47 (2022) 21329–21343, https://doi.org/10.1016/j.ijhydene.2022.04.222.
[40] Y. Sun, Y. Li, S. You, X. Li, Y. Zhang, Z. Cai, M. Liu, N. Ren, J. Zou, $Fe_3C/CoFe_2O_4$ nanoparticles wrapped in one-dimensional MIL-53(Fe)-derived carbon nanofibers as efficient dual-function oxygen catalysts, Chem. Eng. J. 424 (2021) 130460, https://doi.org/10.1016/j.cej.2021.130460.
[41] L. Wang, J. Huang, Z. Huang, H. Li, T. Taylor Isimjan, X. Yang, Revealing dynamic structural evolution of V and P co-doping-induced Co defects as large-current water oxidation catalyst, Chem. Eng. J., 472 (2023) 144924, 10.1016/j.cej.2023.144924.
[42] H. Yu, L. Wang, H. Li, Z. Luo, T.T. Isimjan, X. Yang, Improving the electrocatalytic activity of a nickel-organic framework toward the oxygen evolution reaction through vanadium doping, Chem. Eur. J. 28 (2022) e202201784.
[43] H. Huang, D. Yu, F. Hu, S.-C. Huang, J. Song, H.-Y. Chen, L.L. Li, S. Peng, Clusters induced electron redistribution to tune oxygen reduction activity of transition metal single-atom for metal-air batteries, Angew. Chem. Int. Ed. 61 (2022) e202116068, https://doi.org/10.1002/anie.202116068.
[44] R. Zhang, Z. Liu, S. Zheng, L. Wang, L. Zhang, Z.-A. Qiao, Pyridinic nitrogen sites dominated coordinative engineering of subnanometric Pd clusters for efficient alkynes' semihydrogenation, Adv. Mater. 35 (2023) 2209635, https://doi.org/10.1002/adma.202209635.
[45] D. Liu, Q. Zeng, C. Hu, H. Liu, D. Chen, Y. Han, L. Xu, J. Yang, Core-shell CuPd@NiPd nanoparticles: Coupling lateral strain with electronic interaction toward high-efficiency electrocatalysis, ACS Catal. 12 (2022) 9092–9100, https://doi.org/10.1021/acscatal.2c02274.
[46] B. Yang, W. Zhang, S. Hu, C. Liu, X. Wang, Y. Fan, Z. Jiang, J. Yang, W. Chen, Bidirectional controlling synthesis of branched PdCu nanoalloys for efficient and robust formic acid oxidation electrocatalysis, J. Colloid Interface Sci. 600 (2021) 503–512, https://doi.org/10.1016/j.jcis.2021.05.018.
[47] F. Luo, Y. Yu, X. Long, C. Li, T. Xiong, Z. Yang, Boosting catalytic activity toward methanol oxidation reaction for platinum via heterostructure engineering, J. Colloid Interface Sci. 656 (2024) 450–456, https://doi.org/10.1016/j.jcis.2023.11.077.
[48] S. Zhuang, D. Chen, Q. You, W. Fan, J. Yang, Z. Wu, Thiolated, reduced palladium nanoclusters with resolved structures for the electrocatalytic reduction of oxygen, Angew. Chem. Int. Ed. 61 (2022) e202208751, https://doi.org/10.1002/anie.202208751.
[49] F. Shahbazi Farahani, M.S. Rahmanifar, A. Noori, M.F. El-Kady, N. Hassani, M. Neek-Amal, R.B. Kaner, M.F. Mousavi, Trilayer metal-organic frameworks as multifunctional electrocatalysts for energy conversion and storage applications, J. Am. Chem. Soc. 144 (2022) 3411–3428, https://doi.org/10.1021/jacs.1c10963.
[50] Y. Mun, S. Lee, K. Kim, S. Kim, S. Lee, J.W. Han, J. Lee, Versatile strategy for tuning ORR activity of a single Fe-N_4 site by controlling electron-withdrawing/donating properties of a carbon plane, J. Am. Chem. Soc. 141 (2019) 6254–6262, https://doi.org/10.1021/jacs.8b13543.
[51] Y. Ruan, H. Lei, W. Xue, T. Wang, S. Song, H. Xu, Y. Yu, G.-R. Zhang, D. Mei, Cu-N-C assisted MnO nanorods as bifunctional electrocatalysts for superior long-cycle Zn-air batteries, J. Alloys Compd. 934 (2023) 167781, https://doi.org/10.1016/j.jallcom.2022.167781.
[52] Y. Zhang, Y. Jiang, G. Jiang, T. Or, R. Gao, H. Zhang, Z. Bai, N. Chen, Y.-P. Deng, Z. Chen, Ordered mesoporous Fe_2N_x electrocatalysts with regulated nitrogen vacancy for oxygen reduction reaction and Zn-air battery, Nano Energy 115 (2023) 108672, https://doi.org/10.1016/j.nanoen.2023.108672.
[53] L. Wang, Y. Qin, H. Li, Z. Huang, M. Gao, T.T. Isimjan, X. Yang, Oxygen vacancy engineering of mesoporous Bi-Fe_2O_3@NC multi-channel microspheres for remarkable oxygen reduction and aqueous/flexible Zn-air batteries, J. Colloid Interface Sci. 650 (2023) 719–727, https://doi.org/10.1016/j.jcis.2023.07.033.
[54] P. Zhang, K. Chen, J. Li, M. Wang, M. Li, Y. Liu, Y. Pan, Bifunctional single atom catalysts for rechargeable zinc-air batteries: From dynamic mechanism to rational design, Adv. Mater. 35 (2023) 2303243, https://doi.org/10.1002/adma.202303243.
[55] W. Zhang, J. Li, Z. Wei, Carbon-based catalysts of the oxygen reduction reaction: Mechanistic understanding and porous structures, Chin. J. Catal. 48 (2023) 15–31, https://doi.org/10.1016/S1872-2067(23)64427-4.